Diagnosing health in composite battery electrodes with explainable deep learning and partial charging data

Ruan, H., Kirkaldy, N., Offer, G. J. & Wu, B.

Original citation:
Ruan, H, Kirkaldy, N, Offer, GJ & Wu, B 2024, 'Diagnosing health in composite battery electrodes with explainable deep learning and partial charging data', Energy and AI, vol. 16, 100352.
https://dx.doi.org/10.1016/j.egyai.2024.100352

DOI 10.1016/j.egyai.2024.100352
ISSN 2666-5468

Publisher: Elsevier

Energy and AI 16 (2024) 100352

Contents lists available at ScienceDirect

Energy and AI

journal homepage: www.sciencedirect.com/journal/energy-and-ai

Diagnosing health in composite battery electrodes with explainable deep learning and partial charging data

Haijun Ruan [a,b,*], Niall Kirkaldy [c,d], Gregory J. Offer [c,d], Billy Wu [a,d,*]

[a] Dyson School of Design Engineering, Imperial College London, SW7 2AZ, London, UK
[b] Centre for E-Mobility and Clean Growth Research, Coventry University, Coventry, CV1 5FB, UK
[c] Department of Mechanical Engineering, Imperial College London, SW7 2AZ, London, UK
[d] The Faraday Institution, Harwell Science and Innovation Campus, OX11 0RA, Didcot, UK

HIGHLIGHTS

- Deep learning health diagnostic framework to quantify composite electrode aging.
- Rapid and transparent health diagnostics while requiring low experimental data.
- Sensitivity analysis determines a physically informed appropriate voltage window.
- The Grad-CAM approach provides explainable insights into how these CNNs work.
- Robustness was validated which works well with the voltage noise of up to 10 mV.

GRAPHICAL ABSTRACT

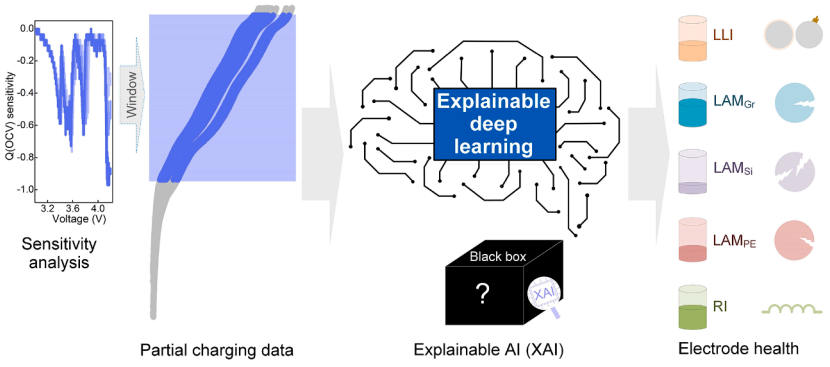

ARTICLE INFO

Keywords:
Lithium-ion battery
Composite electrode
Silicon
Degradation diagnostic
Explainable deep learning
Partial charging

ABSTRACT

Lithium-ion batteries with composite anodes of graphite and silicon are increasingly being used. However, their degradation pathways are complicated due to the blended nature of the electrodes, with graphite and silicon degrading at different rates. Here, we develop a deep learning health diagnostic framework to rapidly quantify and separate the different degradation rates of graphite and silicon in composite anodes using partial charging data. The convolutional neural network (CNN), trained with synthetic data, uses experimental partial charging data to diagnose electrode-level health of tested batteries, with errors of less than 3.1% (corresponding to the loss of active material reaching ~75%). Sensitivity analysis of the capacity-voltage curve under different degradation modes is performed to provide a physically informed voltage window for diagnostics with partial charging data. By using the gradient-weighted class activation mapping approach, we provide explainable insights into how these CNNs work; highlighting regions of the voltage-curve to which they are most sensitive. Robustness is validated by introducing noise to the data, with no significant negative impact on the diagnostic accuracy for noise levels below 10 mV, thus highlighting the potential for deep learning approaches in the diagnostics of lithium-ion battery performance under real-world conditions. The framework presented here can be generalised

* Corresponding authors at: Dyson School of Design Engineering, Imperial College London, SW7 2AZ, London, UK.
E-mail addresses: h.ruan@imperial.ac.uk, haijun.ruan@coventry.ac.uk (H. Ruan), billy.wu@imperial.ac.uk (B. Wu).

https://doi.org/10.1016/j.egyai.2024.100352

Available online 27 February 2024

to other cell formats and chemistries, providing robust and explainable battery diagnostics for both conventional single material electrodes, but also the more challenging composite electrodes.

1. Introduction

Lithium-ion batteries are essential in e-mobility, electronic devices, and grid-level energy storage. Their energy densities have steadily increased year after year, enabled by advances in manufacturing [1] and the introduction of superior electrode materials [2–3]. Lithium-ion batteries with composite anodes consisting of high specific capacity silicon blended with graphite (Gr-Si), and nickel-rich nickel manganese cobalt oxide (NMC) cathodes, are regarded as one of the most promising chemistries [4]; with energy density reaching ~270 $Wh{\cdot}kg^{-1}$. However, widespread adoption still has barriers [5], in part due to the complicated and coupled degradation mechanisms involved in blended anodes which negatively impacts predictability.

Commonly used battery diagnostic techniques include differential capacity/voltage methods which can identify degradation modes (DMs) such as loss of lithium inventory (LLI) and loss of active material in the negative and positive electrodes (LAM_{NE}, LAM_{PE}). For composite Gr-Si anodes, Anseán et al [6]. explored how the incremental capacity (IC) peaks for these batteries can be deconvoluted and how they evolve with different aging modes, however the quantification of Gr and Si degradation was not presented. Schindler et al [7]. and Bazlen et al [8]. analysed the differential voltage (DV) peaks to quantify the DMs but used the full discharge curves, which are seldom found in real-world applications. Kirkaldy et al [9]. presented an open circuit voltage (OCV) fitting method to separate the amount of degradation in Gr-Si composite electrodes, but again focused on full-discharge data. Furthermore, almost all the quantitative diagnostics [6–9] for Gr-Si composite electrodes utilize discharging data rather than charging data, which often is more accessible in real-world conditions.

Several efforts have been made at diagnosing battery health with partial charging data. For instance, Tian et al [10]. and Yang et al [11]. utilised machine learning and DV fitting methods to identify DMs of batteries, respectively. However, optimal determination of the partial charging window remains a gap. Marongiu et al [12]. collected voltage data and focused on the plateau regions to track the DMs in lithium iron phosphate batteries but this approach was only validated with non-composite anodes. Schmitt et al [13]. investigated the DM diagnostics for Gr-Si batteries using the partial charging data at different current rates by fitting the OCV, however, a fixed anode potential curve is utilised without the separation of the Si and Gr degradation over battery lifetime.

To bridge these gaps, we develop a deep learning approach for rapidly quantifying and decoupling degradation in Gr-Si composite battery anodes with partial charging data. A sensitivity analysis, comparing the OCV curve with different DMs, is conducted to determine an appropriate voltage window for diagnostics. Furthermore, we apply an explainable artificial intelligence approach towards developing conceptual understanding of how the deep learning algorithm identifies the DMs. We find that the traditional OCV matching techniques cannot accurately separate the composite anode degradation using partial charging data, while the proposed explainable deep learning approach works rapidly and transparently, with a diagnostic time of less than 7 ms and alleviation around the opaqueness of black box techniques.

2. Battery health diagnostic framework

2.1. Degradation analysis of batteries with Gr-Si composite anodes

The thermodynamic DMs generally include LLI and (de)lithiated LAMs, all of which have a measurable influence on the battery OCV. As the combination of the identical LLI and delithiated LAM can create the same OCV as the corresponding lithiated LAM [14], we focus on the basic DMs: LLI, LAM_{deGr}, LAM_{deSi}, and LAM_{dePE}, and refer to these LAM quantities as LAM_{Gr}, LAM_{Si}, and LAM_{PE} in the later sections.

Fig. 1 depicts the OCV and available capacity changes under the four basic DMs for batteries with composite Gr-Si anodes. The full-cell OCV is the difference between the positive and negative electrode (PE, NE) potentials, assuming lumped battery resistance (see Methods). We assume the surface potential of Gr and Si particles are identical [9] when applying a low current, with the composite anode capacity the sum of both phases (see Methods).

If LLI occurs, a smaller fraction of the electrodes' capacities are used, due to the shift of the NE's OCV (Fig. 1b). As illustrated in the example of 20% LLI, the stoichiometric offset drives the PE to higher voltages at the end of charge, which could destabilize the cathode [15–16], and cause a noticeable increase in battery capacity, around 2%.

If LAM_{deGr} was the dominant mechanism, the NE voltage would decrease at the end of charge, with an initially small effect on the OCV curve, due to an excess of the NE material. Once the remaining capacity of the NE is lower than the full-cell capacity, the full cell loses significant capacity. Here, Fig. 1c presents the example of 20% LAM_{deGr}, which drives the anode potential to decrease at the high state-of-charge (SOC) and thus cause the usage of excess Si materials.

LAM_{deSi} occurs during charging as a result of particle cracking, or electrical isolation of active materials [17]. The example of 60% LAM_{deSi} is illustrated in Fig. 1d, but surprisingly the full-cell capacity loss is only 2%, primarily attributed to the usage of more of the graphite phase and it's higher mass fraction. Thus, we conclude that the Gr degradation means more Si usage and the Si degradation indicates additional Gr utilization, which highlights the challenge of separating composite anode behaviours.

With 20% LAM_{dePE} (Fig. 1e), the PE receives less charge at the end of discharge, with the steep drop of PE's OCV triggering the full-cell voltage limits sooner. These discussions of the impact of full-cell voltage and capacity loss due to LLI and LAMs provide underpinning insights to understand the complicated degradation of composite electrodes, but it should be mentioned that the quantitates are specific to the electrode balance and composite anode ratio.

2.2. Deep learning diagnostic framework

Fig. 2 presents the proposed deep learning diagnostic framework which uses partial charging data as the input and identifies the component DMs (LLI, LAM_{Gr}, LAM_{Si}, LAM_{PE}, and resistance increase (RI)). The convolutional neural network (CNN) (see details in Methods, Supplementary Fig. S3), learns the features in the partial charging data, towards rapid quantification of battery DMs. This CNN is trained with a large number of datasets, which are synthetically generated using an OCV model (see Methods). This requires low training cost/time, as only the experimental half-cell and full-cell OCVs of fresh batteries are needed. The optimal selection of voltage windows for diagnostics is determined by a sensitivity analysis (see Methods), which investigates the change of OCVs with respect to different DMs. Here, highly sensitive regions will be taken as the appropriate window for diagnostics. In order to gain insight into the CNN based approach (a black box technique), an explainable model, the gradient-weighted class activation mapping (Grad-CAM, see details in Methods) visualization technique is utilised to explore how the trained CNN works and which parts of the input are important for quantification. Therefore, this framework provides a generalised diagnostic approach that can rapidly and transparently quantify composite electrode degradation while requiring low experimental data.

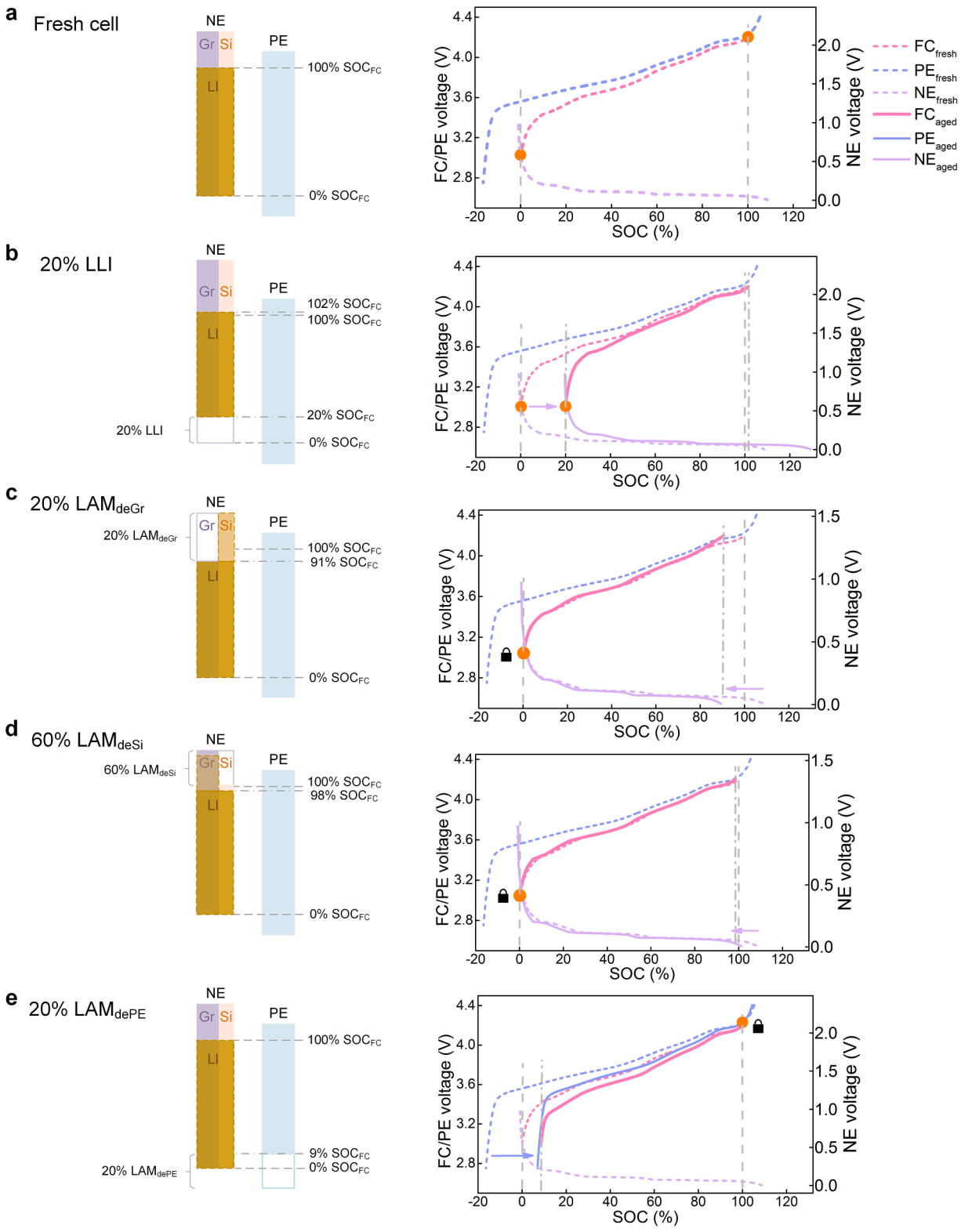

Fig. 1. . Examples of the different DMs for Gr-Si composite batteries. The bars in the left column illustrate the utilization of the electrodes as a result of the DMs, compared to the base case (fresh cell, not to scale). The plots on the right show the corresponding electrode and full-cell (FC) OCVs. The influence of the resistance increase (RI) on the full-cell capacity/resistance and the OCV model parameters are illustrated in Supplementary Fig. S1 and Table S1, respectively. It should be noted that this analysis is based on the current composite anode (Gr fraction: 0.88). The anode potential varies with Gr fractions (Supplementary Fig. S2) and the aging analysis results may be different with various Gr-Si ratios.

3. Results

3.1. OCV model-based sensitivity analysis

As we often take battery voltages as the termination condition during testing, the voltages are generally kept consistent under different aging stages, and we thus transform the OCV-capacity (OCV(Q)) data to capacity-OCV (Q(OCV)) profiles (see Methods). Fig. 3 illustrates the sensitivity of Q(OCV) under four independent DMs, which investigates the change of Q(OCV) curve when varying one DM by a given small percentage while leaving other DMs constant (see Methods), with a high variation of Q(OCV) indicating a high sensitivity.

For LLI, as we make the initial point of charging almost the same, there is a small change of the Q(OCV) in lower voltage regions (3.0–3.4 V), with high sensitivity observed from 3.45–4.2 V. The sensitivity profiles change with different amounts of LLI, which shift to higher voltages, corresponding to the NE movement.

For LAM_{Gr}, the Q(OCV) sensitivity is low in voltage windows from 3.0–4.0 V, except from 3.6–3.85 V, and it is high at the end of charge (4.0–4.2 V), especially for the high LAM_{Gr} (15%, 25%), which corresponds to the lower NE capacity compared to the full-cell capacity.

For LAM_{Si}, there are several peaks in the Q(OCV) sensitivity profiles but these peak values are low compared to the sensitivity due to LLI and LAM_{Gr}. This explains why it is challenging to distinguish the Si degradation. Since the excess Gr materials replace the inactive Si materials to accept/deliver the lithium, the Q(OCV) sensitivity in high voltage areas is still low even with 75% LAM_{Si}. A sensitivity peak is observed at 3.4 V, corresponding to the unique change in the OCV curve at low voltage areas due to the LAM_{Si}.

When the LAM_{PE} is low (i.e. <5%) the sensitivity values are positive, indicating the increase of full-cell capacity due to the lower PE voltage at low SOCs resulting from PE's OCV scaling. With a high LAM_{PE} (i.e. 15%) the sensitivity becomes negative and a high sensitivity is observed from 3.4–4.2 V.

We find the Q(OCV) sensitivity due to the different RI is almost the same, having high values from 3.45 V to 4.15 V (Supplementary Fig. S4a). The sensitivity peaks correspond to the IC peaks, as the resistance shows a strong influence on the OCV plateaus (Supplementary Fig. S4b).

Determining a narrow voltage window for comprehensive diagnostics is highly desirable, yet this needs to cover all the essential sensitive areas of Q(OCV) profiles with respect to all the DMs for good identifiability. With all highlighted sensitive areas in Fig. 3 considered, we select a voltage window from 3.5 V to 4.15 V to quantify the health of each composite electrode.

3.2. Deep learning diagnostics with synthetic data

We generated a dataset for a cell undergoing various degradation pathways, with varying rates of LLI, LAMs, and RI (see Methods), which include 82,810 OCV(Q) curves and this synthetic dataset has defined quantities of each DM, allowing them to be used for CNN training/testing. We trained the CNN with 80% of the data and validated the deep learning approach using the remaining 20% data. Here, the root mean square error (RMSE) and maximal absolute error (MAE) are less than 0.53% and 2.84% (Supplementary Fig. S5, Table S1), respectively, which implies high accuracy of the trained CNN.

We assume two batteries degrade in two different paths, with one showing high Si degradation and another having high Gr degradation (Fig. 4, Supplementary Note 1). With the trained CNN and the partial charging data from 3.5–4.15 V, the DMs are rapidly quantified, which agree well with the target ones (Fig. 4, Table 1), with the RMSE and MAE of less than 1.27% and 2.67%, respectively. This highlights the ability of CNNs in distinguishing the Gr and Si degradation whatever their aging pathways during the whole lifetime are.

3.3. Deep learning diagnostics with experimental data

We validated the trained CNN using the experimental data from a cycle aging study of a commercial cell (LG M50T) which contains a Gr-Si composite NE and NMC811 ($LiNi_{0.8}Mn_{0.1}Co_{0.1}O_2$) PE (see Methods). We first utilize partial experimental charging data to quantify the electrode degradation of real Gr-Si composite cells cycled from 0%−30% SOC, as shown in Fig. 5, with the electrode health identified in 7 ms for each input (tested on a general computer, see Methods). The LAM_{Si} significantly increases in the initial 156 equivalent full cycles, primarily attributed to the Si particle fracture due to the high mechanical stress resulting from the almost full usage of the Si material [17–18]. The cracking exposes new particle surfaces to the electrolyte, leading to the formation of the solid electrolyte interphase (SEI), which results in a high increase of LLI. After 200 cycles, the LAM_{Si} stablises to around 74%; the LLI gradually increases, likely resulting from the SEI growth/formation. The nickel-rich NMC degrades slowly, exhibiting good stability.

With the identified DMs, the full-cell OCV can be reconstructed, and the available capacity and energy of composite electrode cell under different aging states can be estimated. From Fig. 5b and c, we observe that they show good consistency with the measured ones, with the RMSE of 10.40 mV, 0.58%, and 0.57% (Table 2), respectively, implying

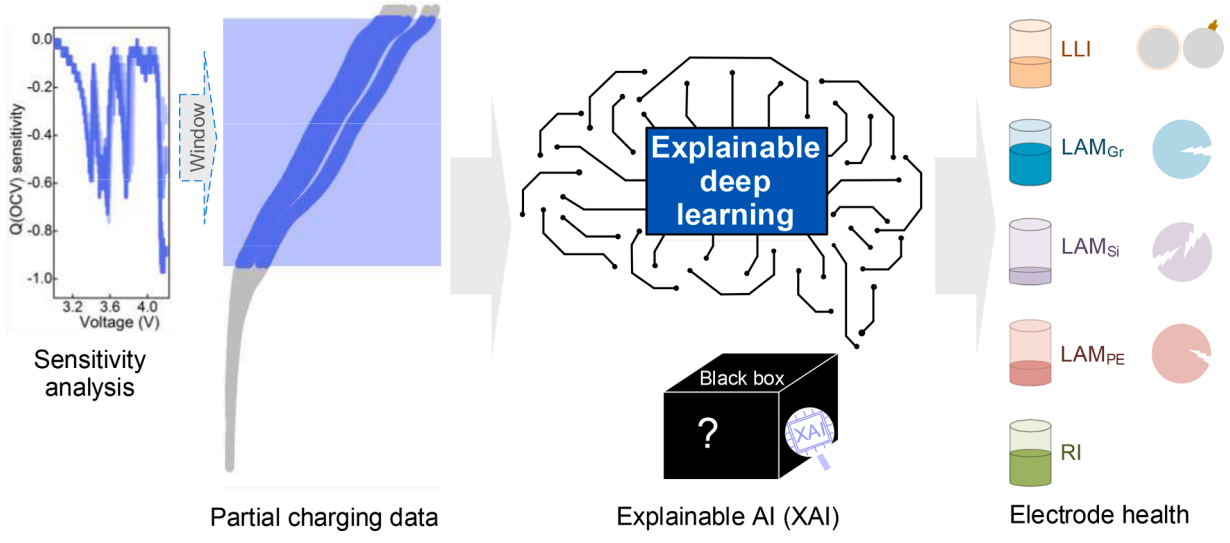

Fig. 2. Overview of the explainable deep learning health diagnostic framework for composite electrode batteries with partial charging data.

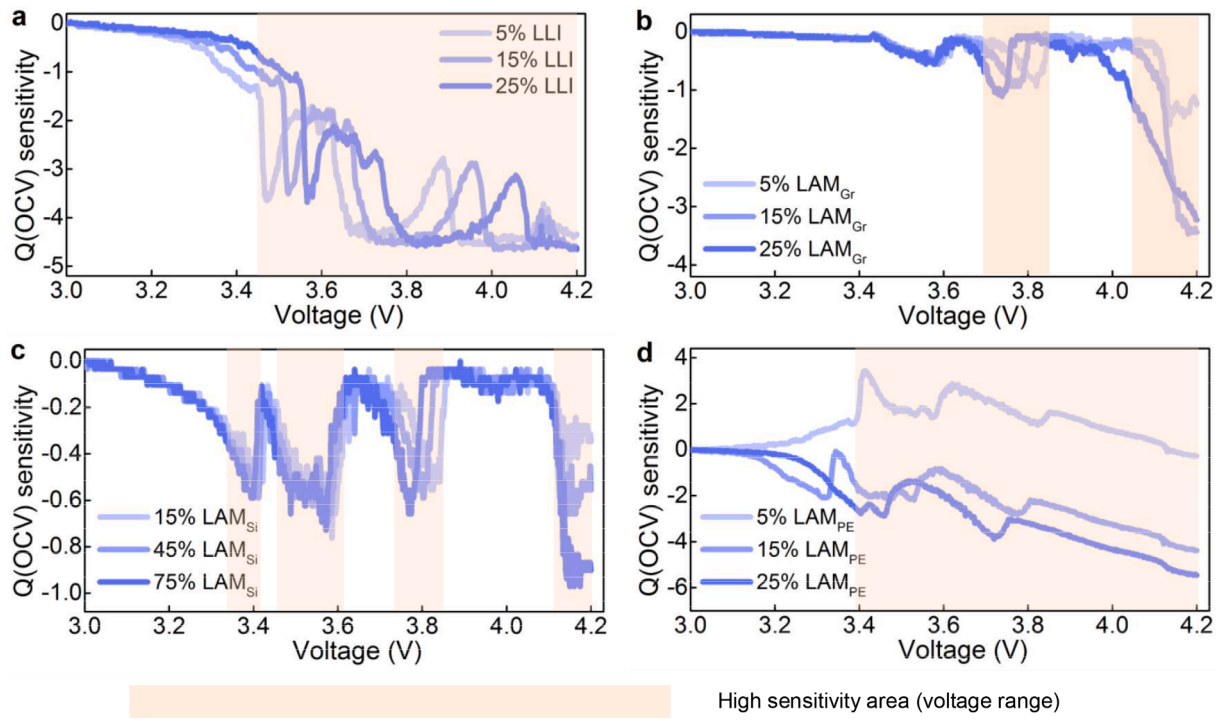

Fig. 3. Sensitivity analysis of Q(OCV) curves under different DMs: a. LLI, b. LAM_{Gr}, c. LAM_{Si}, and, d. LAM_{PE}. The areas highlighted with the color represent the highly sensitive voltage region.

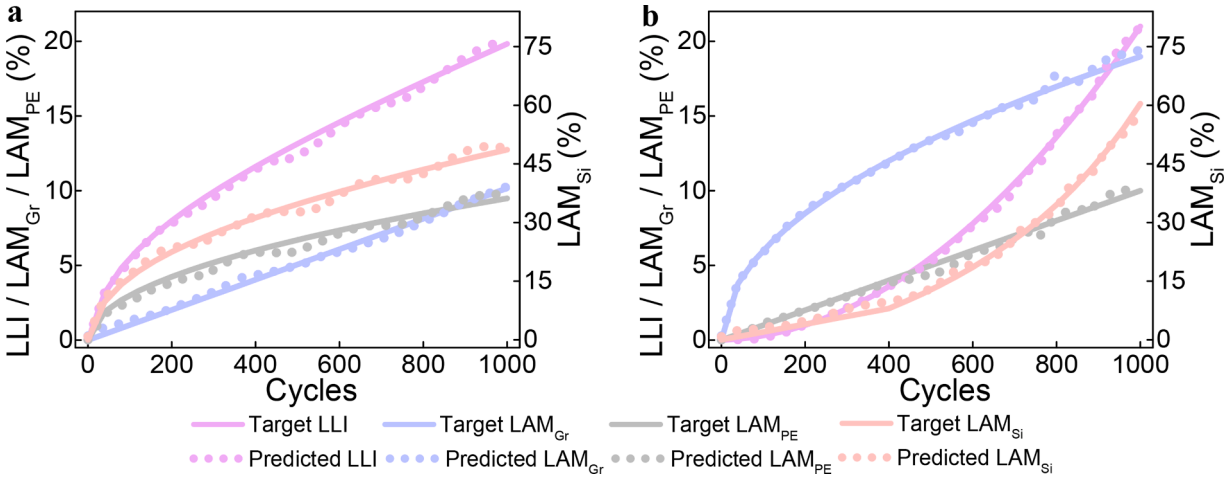

Fig. 4. The diagnostic results with the proposed method using the partial charging data under different degradation paths: a. aging path I, and b, aging path II. The setting degradation modes in two aging paths and the generated OCVs are presented in Supplementary Note 1 and Fig. S5, respectively.

Table 1
The comparison results of the quantified DMs under different assumed aging paths leveraging the trained CNN with respect to the target DMs.

		LLI	LAM_{Gr}	LAM_{Si}	LAM_{PE}
Aging path I	RMSE (%)	0.35	0.24	1.23	0.39
	MAE (%)	0.79	0.50	2.67	0.76
Aging path II	RMSE (%)	0.26	0.31	1.27	0.32
	MAE (%)	0.66	0.90	2.09	0.66

accurate comprehensive health diagnostics using only partial charging data.

We use full charging data to diagnose battery health, with the quantified DMs (Supplementary Fig. S7) considered as the benchmark, and the diagnostic errors using partial data are displayed in Fig. 5d, having an RMSE of less than 3.1% (<0.07 Ah) for all thermodynamic DMs. This highlights the rationality of the selected voltage window using sensitivity analysis.

We investigate the degradation mechanisms of the real Gr-Si composite electrode batteries aged in other conditions, with the quantified DMs using the proposed CNN method and the partial data from 3.5–4.15 V, as shown in Fig. 6. For the battery cycled over the full SOC range, the LAM_{Si} firstly increases and then stablises at ~27%, which is much lower than that in the low SOC cycling, primarily because of the lower silicon activity at high SOCs. LAM_{Gr} is higher than that aged in the low SOC range, likely due to the high mechanical stress when cycling at high SOCs [16,19].

The DMs of the battery aged over the 0–30% SOC range at 40 °C are similar to those at 25 °C but the LLI is higher, primarily attributed to the high SEI growth rate at high temperatures [20], which is validated by a

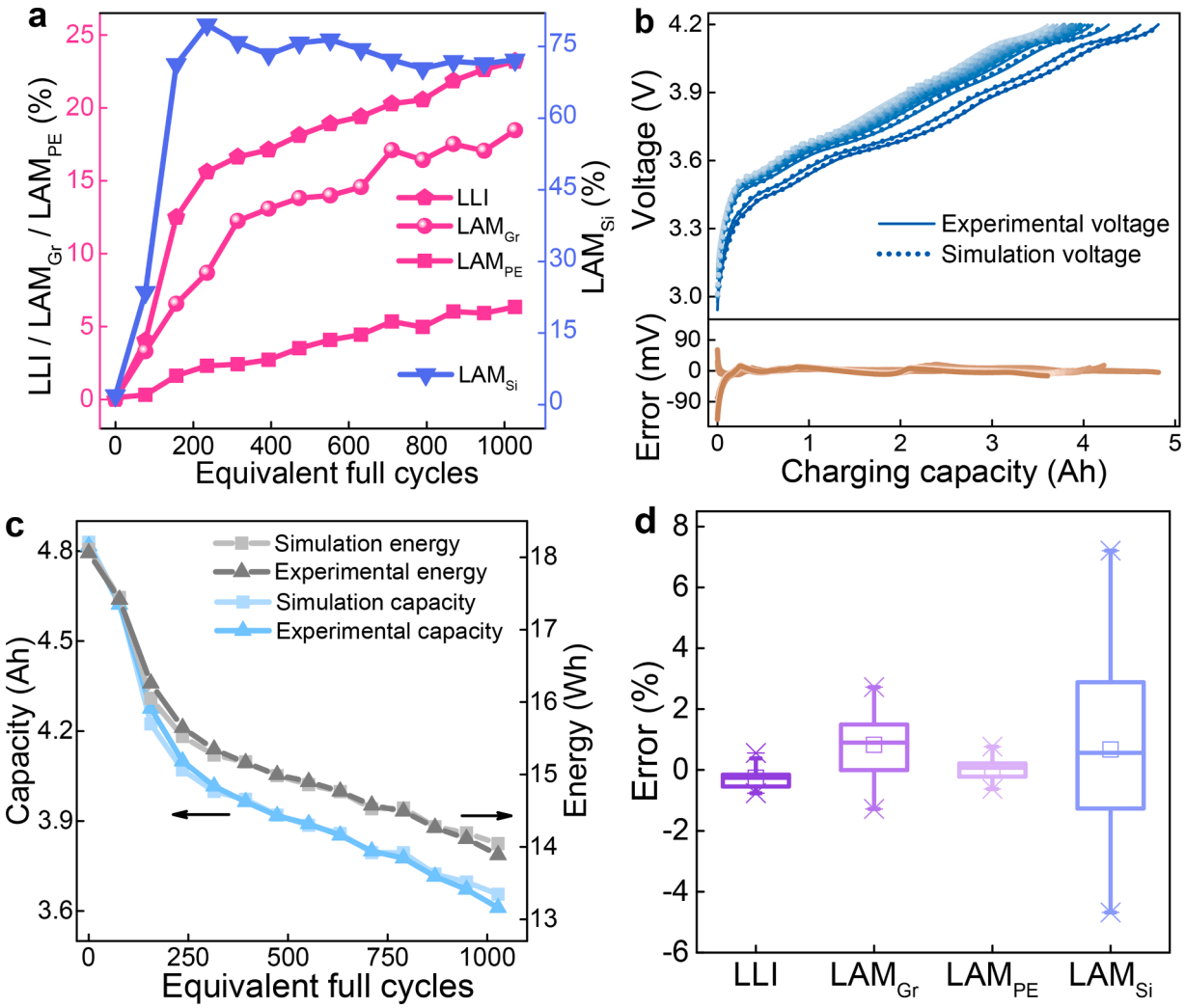

Fig. 5. Comprehensive health diagnostic results: a. quantified DMs; b. reconstructed and experimental OCVs; c. estimated and experimental capacity/energy; d. the errors of identified DMs compared with those using full voltage data. The errors of the diagnostic using partial data compared to that using full data vary with battery aging and we use the box chart to illustrate the error distribution for the whole lifetime diagnostics.

Table 2
The estimation errors of OCVs, capacity and energy using the proposed method.

Batteries	OCV (mV)		Capacity (%)		Energy (%)	
	RMSE	MAE	RMSE	MAE	RMSE	MAE
0–30% SOC, 25 °C	10.40	145.22	0.58	12.50	0.57	1.28
0–100% SOC, 25 °C	13.33	154.20	0.22	4.47	0.24	0.57
0–30% SOC, 40 °C	12.28	159.96	0.73	11.12	0.55	0.81
0–30% SOC, 10 °C	9.92	181.41	0.61	18.29	0.63	1.36

high identified resistance (Supplementary Fig. S8).

The degradation at 10 °C is significantly different, with all the DMs gradually increasing. After 795 cycles, the LAM$_{PE}$ and LLI increase dramatically, leading to a rapid decrease in battery capacity. This fast degradation may be associated with the electrolyte consumption in the cathode areas [16,21], resulting in the available lithium trapped in the inactive lithiated cathode.

We reconstruct the full-cell OCV (Supplementary Fig. S9), and calculate the available capacity and energy of composite electrode batteries using the identified DMs (Fig. 6d), with those agreeing with the measured ones, having the RMSE of 13.33 mV, 0.73%, and 0.63% (Table 2), respectively, which suggests high accuracy of comprehensive diagnostics.

4. Discussion

4.1. Interpreting the CNN

We consider the individual DM to analyze which parts in the input are important to quantify the DMs; exploring how the diagnostic CNN works. The OCVs under each DM (Supplementary Fig. S10) are generated using the OCV model, with the ΔQ(OCV) being the difference between the aged and fresh Q(OCV) (Supplementary Fig. S11). With the ΔQ(OCV) under each DM as the input, we employ the Grad-CAM (see Methods) technique to compute the gradient of a differentiable output with respect to the convolutional features in a last convolutional layer, as shown in Fig. 7a. The parts with a large Grad-CAM value are those that most impact the CNN diagnosing the DMs. The Grad-CAM highlights the input from 3.89–4.12 V, suggesting that the highly varied Q (OCV) at high voltage regions are important for quantifying LLI. This identified voltage range corresponds to the sensitive area of Q(OCV) due to LLI.

The Grad-CAM outputs suggests the 4.12–4.15 V range has the greatest impact for the CNN on quantifying the LAM$_{Gr}$, and the region from 3.75–3.89 V is more important for the LAM$_{Si}$ identification decision of the network, whilst 3.50–3.61 V contributes most to the quantification of LAM$_{PE}$. We find these highlighted areas of the diagnostic CNN are different for identifying independent DMs. Although the Q

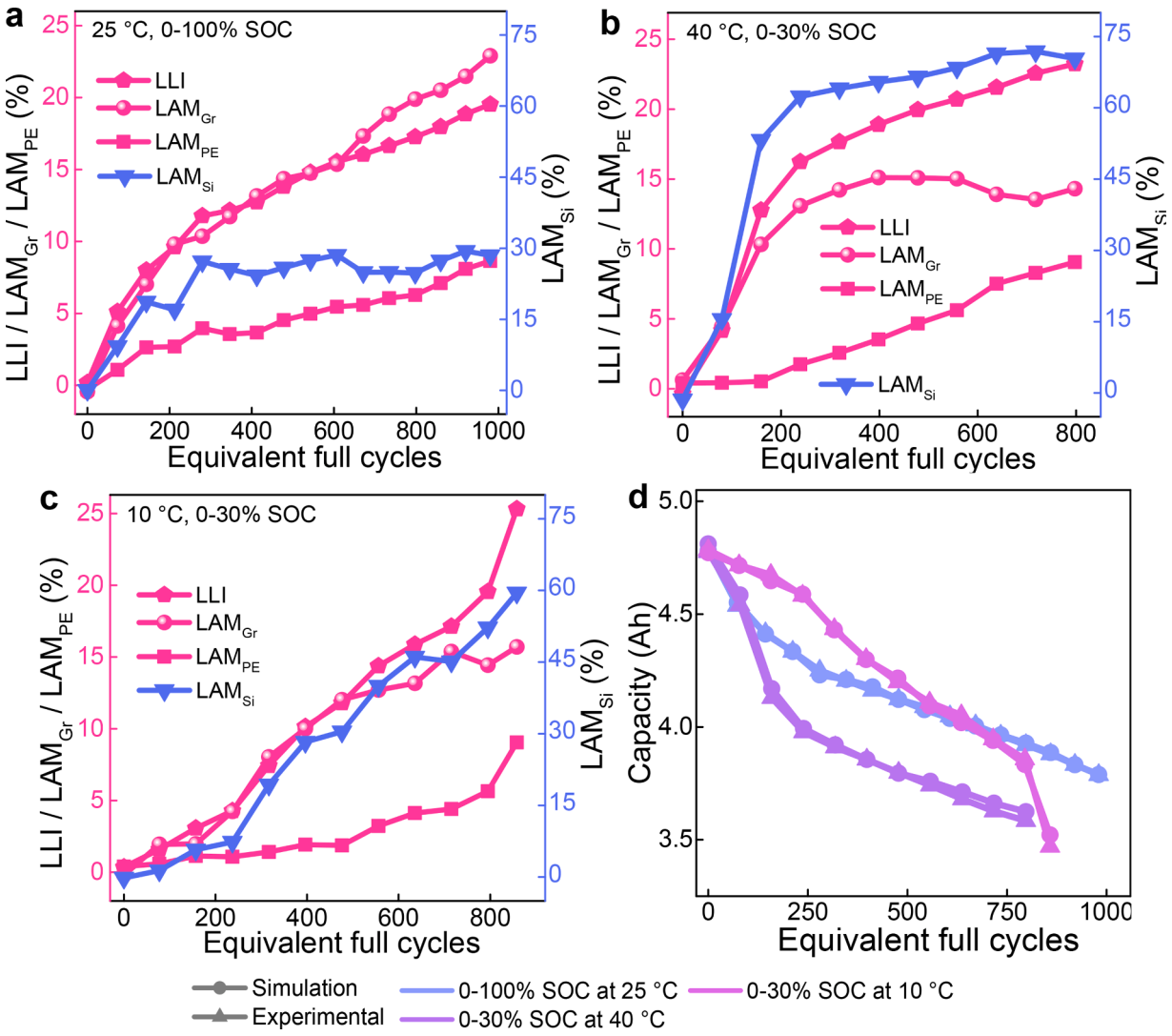

Fig. 6. Comprehensive health diagnostic results: DMs of batteries aged a. in the full SOC range at 25 °C; b. in the 0–30% SOC range at 40 °C; c. in the 0–30% SOC range at 10 °C. d, the estimated and experimental capacity aged under different conditions.

(OCV) sensitivity due to LAM_{Gr} is low, the highly increased sensitivity areas in the high voltage range (near 4.15 V) are identified by the CNN to diagnose LAM_{Gr}. The Q(OCV) sensitivity profiles due to LAM_{Gr} and LAM_{Si} are quite similar but the CNN finds the higher sensitive features (near 3.8 V) to quantify LAM_{Si}. This demonstrates that the highlighted importance, using the Grad-CAM technique, is consistent with the sensitivity analysis, implying a trustable CNN.

4.2. *Diagnostics with different voltage windows*

We investigate the electrode health diagnostics using partial charging data with different voltage windows to validate the sensitivity analysis and check whether the selected voltages are optimal. Here, we take the diagnostic with the full charging data (3.17–4.2 V) as the benchmark, i.e. 'truth'. Firstly, we keep the upper voltage fixed at 4.2 V and change the lower voltage, to investigate how the diagnostic errors of DMs vary. The CNN can accurately identify the LLI under different lower voltages, as shown in Fig. 8, while the quantification of LAM_{Gr} shows a large uncertainty due to the relatively low Q(OCV) sensitivity. When the lower voltage is less than 3.5 V, the CNN can quantify the LAM_{Si}, but when over 3.6 V, the diagnostic error is high, likely because the sensitivity peak from 3.5–3.6 V (Fig. 3c) indicates a key feature of LAM_{Si}. As the Q(OCV) due to LAM_{PE} at low voltage areas changes in different ways, having a positive sensitivity sometimes and a negative value in other cases, the uncertainty of identifying the LAM_{PE} increases, with the increase of the lower voltage.

When decreasing the upper limit of the voltage window, the LLI and LAM_{PE} errors are low, while the LAM_{Gr} error increases, having a mean error of about 2% with the upper voltage of 4.10 V, as Q(OCV) in the high voltage area is more sensitive to LAM_{Gr}, especially when the anode limits the full-cell capacity. With a low upper voltage, such as 4.05 V, the identification error of LAM_{Si} is high, and the errors of all the DM increase. Therefore, we can conclude that the lower and upper voltages of 3.5 V and 4.15 V respectively are the optimal partial voltage window that can be used for electrode health diagnostics.

4.3. *Diagnostic comparison with the OCV fitting*

We utilize partial charging data to parameterise an OCV model with the particle swarm optimization method [14] and identify the DMs, with the diagnostic results illustrated in Fig. 9. The quantified LLI and LAM_{PE} are almost the same as those in the benchmark, respectively, while the identified LAM_{Gr} and LAM_{Si} are significantly different, having a low LAM_{Si} (~10%) and a high LAM_{Gr} (~30%), thereby attributing the initial fast degradation of batteries to the LAM_{Gr}. On the other hand, the OCV matching approach using the full voltage data gets similar diagnostic

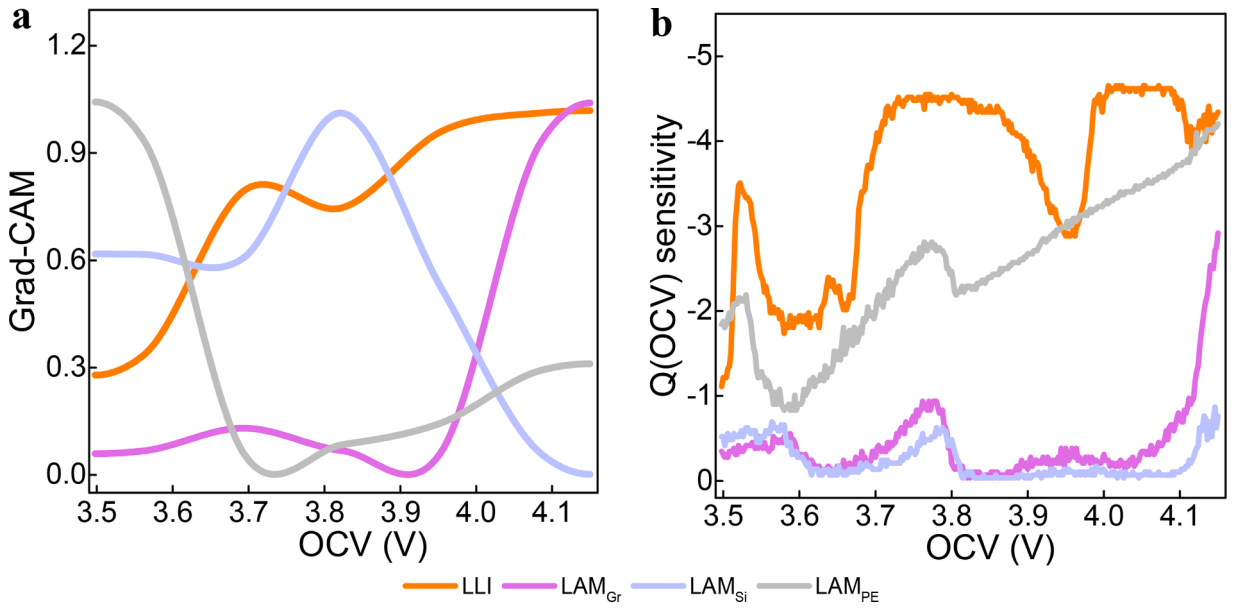

Fig. 7. The interpretation of how the diagnostic CNN works. a. The calculated Grad-CAM for the trained CNN using the ΔQ(OCV), and b. the Q(OCV) sensitivity due to 15% LLI, 15% LAM_{Gr}, 60% LAM_{Si}, and, 15% LAM_{PE}.

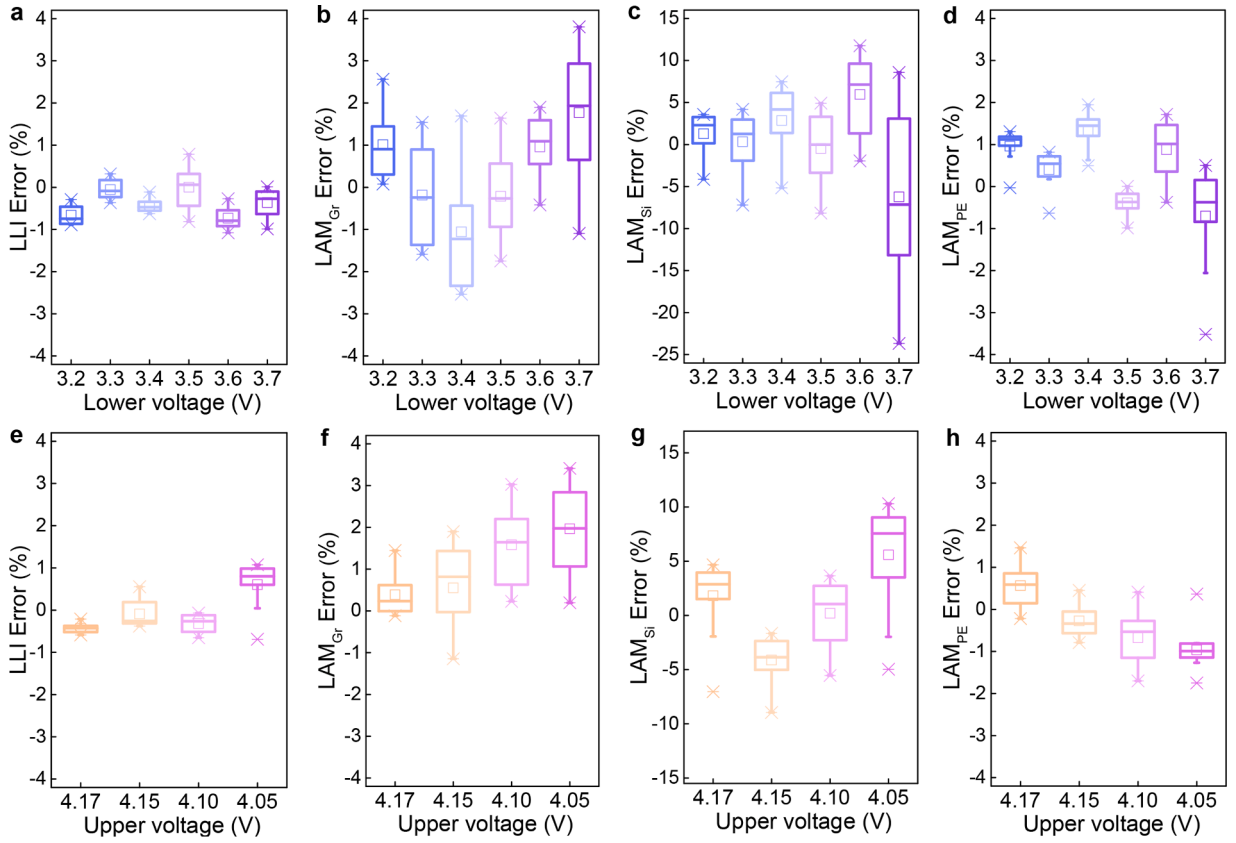

Fig. 8. Electrode health diagnostic errors for: a, LLI, b, LAM_{Gr}, c, LAM_{Si}, and d, LAM_{PE}, with different lower voltages while keeping the upper voltage at 4.2 V; and e, LLI, f, LAM_{Gr}, g, LAM_{Si}, and h, LAM_{PE}, with different upper voltages and the constant lower voltage at 3.17 V, when compared the DM quantification that employed the full voltage data from 3.17V-4.2 V. The errors of the diagnostic using partial data with different lower/upper limits compared to that using full data vary with battery aging and we use the box chart to illustrate the error distribution for the whole lifetime diagnostics.

results (Supplementary Fig. S12) to those in the benchmark. This demonstrates that the OCV-fitting method has challenges when separating the Gr and Si with the partial data.

Despite the excellent fitting of the OCV within the partial voltage window, with an RMSE of less than 3.5 mV (Fig. 9b, Table 3), a significant deviation between the simulation and experimental OCVs is observed when extending the simulated OCV across the full voltage range (Fig. 9c), having an RMSE of ~31 mV. This indicates the over

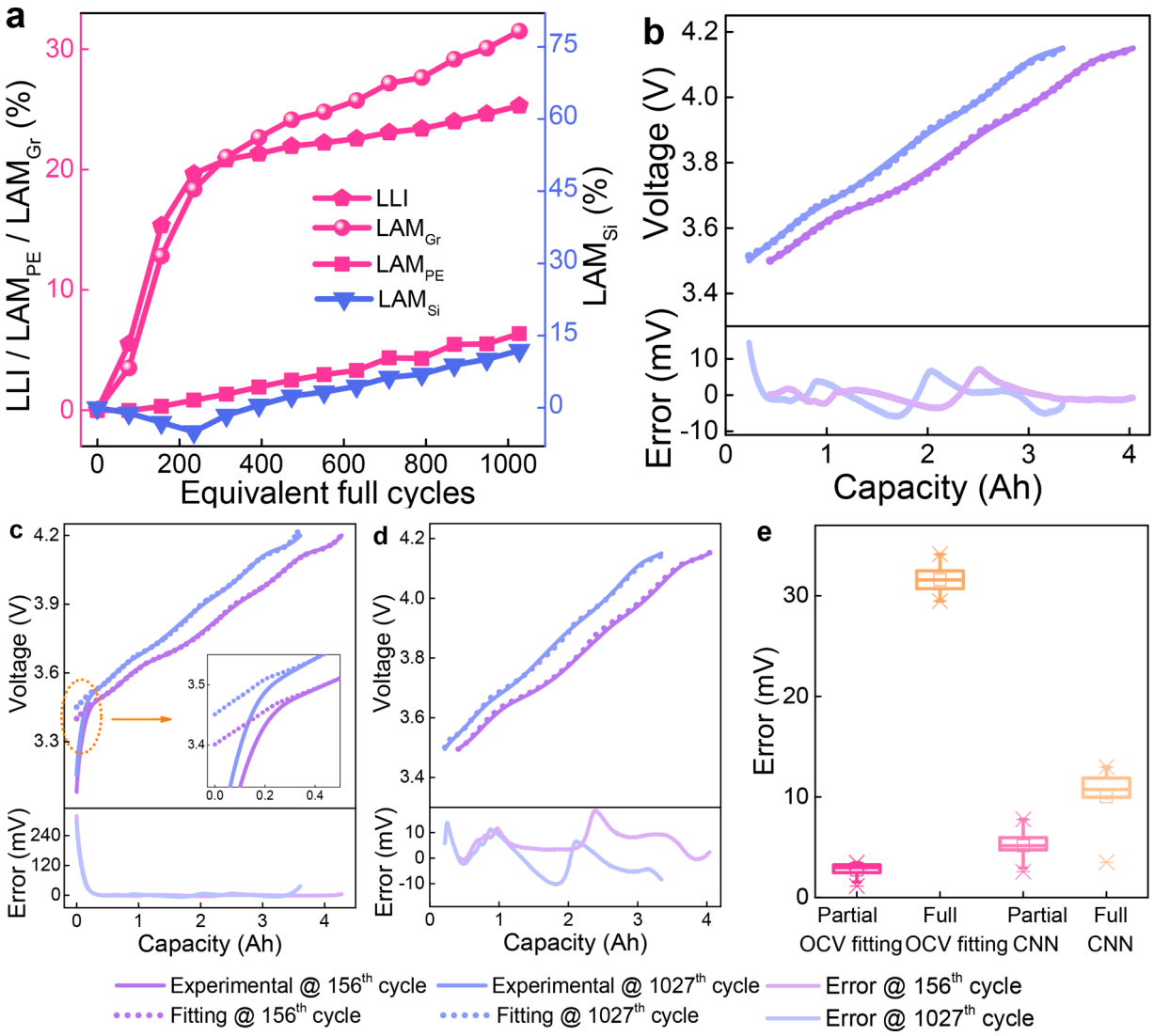

Fig. 9. a, Health diagnostic with the OCV fitting method using partial voltage data; the experimental OCV and simulation OCV calculated with the identified parameters using the OCV fitting method as well as the simulation error for b, the partial voltage window, c, the full voltage window; d, the experimental OCV and simulation partial OCV calculated with the identified parameters using the proposed method; e, The simulation OCV errors for the partial and full voltage data.

Table 3
The errors between the simulation and experimental OCVs at the 156th and 1027th cycles when using different diagnostic methods.

		OCV (mV) from 3.5–4.15 V		OCV (mV) from 3.17–4.2 V	
		RMSE	MAE	RMSE	MAE
156th cycle	OCV fitting	2.23	7.25	30.98	319.38
	Proposed method	7.77	18.72	10.42	82.00
1027th cycle	OCV fitting	3.46	14.50	30.87	296.43
	Proposed method	5.95	13.97	12.97	145.22

fitting happened when using the partial data, and the OCV fitting method is difficult to effectively capture the small key features of different DMs.

In comparison, using the identified DMs with the proposed method, the OCV simulation errors are slightly higher for the partial data (Fig. 9d) but far lower in the full voltage range (Figs. 5b and 9e). This confirms that the developed CNN can effectively distinguish the key features of OCVs despite the partial data used.

4.4. Diagnostics with noisy data

In real-world applications, it's likely there will be voltage measurement errors when sampling the charging data; to replicate this, we altered the OCV data by adding random noises at different amplitudes, from 5 mV to 20 mV. This allowed us to inspect the effect of the noisy data on the ability of the diagnostic method to accurately determine the DMs. Fig. 10 displays the diagnostic results with different levels of noise, with low noise (<10 mV) having a minimal impact on the diagnostic ability. When the noise is higher than 15 mV, the quantification errors of LAM_{Si} and LAM_{Gr} become large, primarily due to their low sensitivity to OCV profiles. We can conclude that the proposed diagnostic is capable of tolerating the noise of up to 10 mV, highlighting the promising potential for diagnosing electrode health in the real world.

4.5. Prospects

We employed explainable AI to diagnose electrode health while providing underpinning knowledge of how the AI works, which facilitates the optimization of the diagnostics. For example, the useful data features highlighted by the Grad-CAM technique can be directly used as the input of diagnostics; reducing the data required for diagnostics.

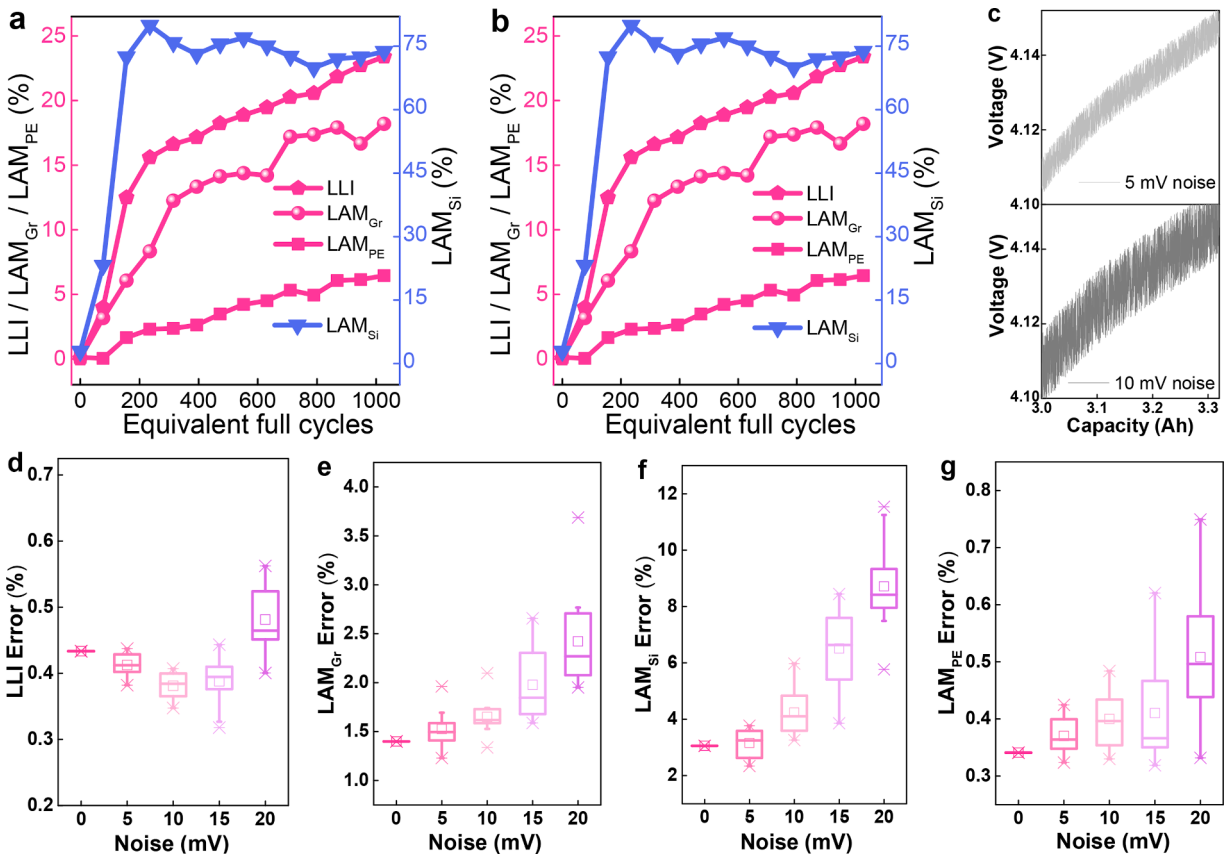

Fig. 10. Electrode health diagnostics with the experimental data when adding random noises of a, 5 mV, b, 10 mV; c, The partial OCV(Q) data at the 1027th cycles when adding random noises of 5 mV and 10 mV; The diagnostic errors for: d, LLI, e, LAM_{Gr}, f, LAM_{Si}, and g, LAM_{PE} with adding different noises, when compared the DM quantification that employed the full voltage data from 3.17V-4.2 V.

The proposed approach exhibits promising performance characteristics which are not limited to the studied NMC811/Gi-Si batteries; being chemistry and cell design agnostic. With the half-cell data of whatever the materials are, we can develop the OCV model and explainable deep learning diagnostics through referring to the proposed method. Therefore, this approach, using sensitivity analysis and explainable machine learning to identify voltage windows for decoupling the degradation modes should work with any cell and chemistry, and provides a useful tool for battery charge optimization, lifetime extension and safety monitoring algorithms

5. Conclusions

We propose a deep learning health diagnostic framework that uses partial charging data to quantify and decouple degradation modes in lithium-ion batteries with composite graphite-silicon anodes in 7 ms using a general purpose computer. The deep learning model is trained with synthetic data, which requires only full-cell and half-cell OCVs of fresh batteries rather than extensive experimental aging data. This is subsequently validated with experimental aging data, with the diagnosing errors of less than 3.1% compared to the identified electrode capacity using full data. We utilize the gradient-weighted class activation mapping method to explain how the convolutional neural network works when diagnosing electrode health. We find that the unique feature for each degradation mode can be learnt by the deep learning approach, which highlights the model transparency and explainability. Comparison with the standard OCV-fitting method further demonstrates that the developed approach can effectively identify the important features of each electrode material.

By exploring the Q(OCV) sensitivity under each degradation mode, we identify the high sensitivity regions for each electrode degradation mode, providing a physical approach for determining the appropriate voltage window for diagnostics with partial charge data. We verified those results by performing the diagnostics on different partial charging voltage windows and via deep learning interpretation, confirming the effectiveness of sensitivity analysis to find the optimal partial voltage ranges.

The Gr-Si composite battery cycled at room/elevated temperatures and low SOC range shows high Si degradation due to the particle cracking because of the high mechanical stress, and the resulting available lithium loss, from the SEI formation and growth. Cycling over full SOC range, the lower Si loss is found but with higher levels of Gr degradation, likely attributed to the unstable structure at this SOC range and larger concentration gradients forming during cycling. For the battery aged at low temperature and low SOC range, the degradation is significantly different, with all the electrode degradation proceeding slowly at first before increasing rapidly, possibly as a result of electrolyte dry out.

The robustness of the proposed method is validated by introducing noise to the data, with no significant negative impact on the diagnostic for noise levels below 10 mV. The findings in this paper, thus provide new insights and new approaches for real-world diagnostics of lithium-ion batteries with composite graphite-silicon anodes. The general approach of using explainable machine learning to help understand the voltage windows within which the consequences of different degradation mechanisms are most observable, should also be applicable to other degradation mechanisms, cells and chemistries.

6. Methods

6.1. Battery experiments

High-energy density commercial 21,700 cylindrical cells (LG M50T, LG GBM50T2170, the diameter: 21 mm, and height: 70 mm, Supplementary Fig. S13), composed of a SiO_x-doped graphite negative electrode alongside an NMC-811 positive electrode, with a nominal capacity of 5.0 Ah (18.2 Wh), were cycled at different temperatures and SOC ranges. During charging, the Li^+ moves from cathode to the anode and the Gr and Si are competing to get the $Li^+$and electron for the electrochemical reactions, with the following Li diffusion processes. Generally, the Si is active in the low SOC areas. When discharging, the Li^+ and electron moves from anode to the cathode. Three cells were tested in the low SOC range from 0–30% at 10 °C, 25 °C and 40 °C; they were charged by 1.5 Ah at 0.3 C and discharged to 2.5 V at 1 C. One cell was aged over the full SOC range (0–100%); it was charged to 4.2 V at 0.3 C, holding until the current was lower than 50 mA, and discharged to 2.5 V at 1C.

Each aging set consisted of a fixed number of aging cycles (78 cycles for the 0–100% SOC cell, and 257 cycles for the 0–30% SOC cells); these are roughly equivalent in terms of equivalent full cycles ($257\times0.3\approx78$). After each aging set, the cells were characterised using a reference performance test which was always performed at 25 °C. This test included a full discharge/charge cycle at 0.1C; the cells were discharged to 2.5 V at 0.1C, rested under open-circuit conditions for 6 h, then charged to 4.2 V at 0.1C, with a CV hold at 4.2 V until the current dropped below 50 mA. The 0.1C charging data was used in the DM analyses described in this paper. After the performance test, cells would be subject to another aging set (as described above), with this procedure repeated until the cells reached end-of-life. The detailed testing procedure and the accompanying data can be found in the references [9, 22].

6.2. OCV model

We modified our previously developed OCV model [14] for composite batteries, considering the graphite and silicon materials to be connected in parallel, which allows the OCV of batteries with the Gr-Si composite anode to be expressed as:

$$\begin{cases} U_{\mathrm{Cell}} = U_{PE}(x_{PE}) - U_{NE}(x_{NE}) - IR \\ x_{PE} = x_{PE,0} - \int_0^t \frac{I}{Q_{PE}} d\tau \\ x_{NE} = x_{NE,0} + \int_0^t \frac{I}{Q_{NE}} d\tau \\ X_{\mathrm{NE}}(V) = \lambda \cdot X_{\mathrm{Gr}}(V) + (1-\lambda)\cdot X_{\mathrm{Si}}(V) \\ U_{NE}(x_{NE}) = f^{-1}(X_{NE}(V)) \end{cases} \tag{1}$$

where subscripts *PE, NE, Gr, Si*, and Cell indicate the positive electrode, negative electrode, graphite, silicon, and the battery with the Gr-Si composite anode, respectively, and *U, x, Q, λ*, and *X* represent the OCV, stoichiometric coefficient, maximum available capacity, the ratio of graphite capacity with respect to the total NE capacity, and the normalised capacity, respectively. $x_{PE,0}$ and $x_{NE,0}$, stand for the values of x_{PE} and x_{NE} corresponding to the 0% SOC in the full cell, respectively. The currents $I > 0$ and $I < 0$ denote a discharge and charge processes, respectively, and *R* indicates an additional potential loss for the full cell constructed from the half cells of PE and NE, corresponding to the resistance in the full cell.

When parameterizing the OCV model, not only the errors of the OCV (Q) but also the deviations of their differentials are taken into account. The differential signals, such as the IC and DV, highlight the key information of electrode transition processes [23] and thus they aid the accuracy of the OCV model by focusing on spectra that are more sensitive to PE and NE processes, respectively. We consider the objective function as:

$$\begin{cases} f_{obj_{OCV}} = \omega_U \cdot U_{RMSE} + \omega_{IC} \cdot IC_{RMSE} + \omega_{DV} \cdot DV_{RMSE} \\ U_{RMSE} = \sqrt{\frac{1}{T}\sum_{t=1}^{T}\left(U_{\mathrm{cell}_{sim}}(t) - U_{\mathrm{cell}_{\exp}}(t)\right)^2} \\ IC_{RMSE} = \sqrt{\frac{1}{N_1}\sum_{\mathrm{n}=1}^{N_1}\left(IC_{U_{\mathrm{cell}_{sim}}}(n) - IC_{U_{\mathrm{cell}_{\exp}}}(n)\right)^2} \\ DV_{RMSE} = \sqrt{\frac{1}{N_2}\sum_{\mathrm{n}=1}^{N_2}\left(DV_{U_{\mathrm{cell}_{sim}}}(n) - DV_{U_{\mathrm{cell}_{\exp}}}(n)\right)^2} \end{cases} \tag{2}$$

where ω_U, ω_{IC}, and ω_{DV} stand for the weighting coefficients for the RMSEs of OCV, IC, and DV, respectively.

6.3. Sensitivity analysis

In the OCV model, we take the full-cell OCV as the output and the DM as the input. A sensitivity coefficient ($\phi_{i,j}$) measures the ratio of the change in output (Y_j) to the change in input (X_j) [24–25], while holding all other parameters fixed. The sensitivity coefficient ($\phi_{i,j}$) can thus be approximated as the partial derivative:

$$\phi_{i,j} = \frac{\partial Y_j}{\partial X_i} \tag{2a}$$

where subscripts *i* and *j* indicate one of five DMs and the data points in the Q(OCV) curve, respectively. We consider the Q(OCV) data and the sensitivity coefficient can thus be written as:

$$\phi_{i,j,k} = \frac{\Delta Q_j}{\Delta \mathrm{DM}_{i,k}} \tag{3}$$

We consider several small changes (represented by the subscript *k*) in the DM_i, e.g. $\Delta\mathrm{DM}_i=\pm0.5\%, \pm0.25\%$, and calculate the mean sensitivity coefficient, described as:

$$\widetilde{\phi}_{i,j} = \frac{1}{N}\sum_{N}\phi_{i,j,k} \tag{4}$$

6.4. Data generation and transformation

We assume that the maximum values of LLI, $\mathrm{LAM_{Gr}}$, and $\mathrm{LAM_{PE}}$ are 24% when synthetically generating data, and they varied from 0% to 24% with 4%, 2%, and 4% increment, respectively. The maximum values of $\mathrm{LAM_{Si}}$ and RI are 84% and 120%, changing with 7% and 10% increment, respectively. With different values of five independent DMs, the dataset for battery degradation included 82,810 independent combinations, so we synthesized 82,810 unique OCVs with the half-cell potentials of PE and NE using Eq. (1). The synthetic OCV dataset would cover almost all aging paths [14], when the battery capacity loss and resistance increase are less than 20% and 120%, respectively.

We considered the experimental full-cell OCV(Q) data as the capacity as a function of voltage (Q(OCV)), using Eq. (5) for data transformation, as there are plenty of data points in the OCV(Q) data due to the low current measurement.

$$Q_j(V_j) = \mathrm{median}[Q(V)], \mathrm{V}_j - \Delta\mathrm{V} \le \mathrm{V} \le \mathrm{V}_j + \Delta\mathrm{V} \tag{5}$$

For the CNN input, to highlight the Q(OCV) variation with respect to the initial Q(OCV) of fresh batteries, we considered the ΔQ(OCV), expressed as:

$$\Delta Q(OCV) = Q_{\text{aged}}(OCV) - Q_{\text{fresh}}(OCV) \quad (6)$$

where $Q_{\text{aged}}(OCV)$, and $Q_{\text{fresh}}(OCV)$ represent the Q(OCV) of aged and fresh batteries, respectively.

To standardize the capacity-voltage (Q(OCV)) data, the capacity was evaluated at 600 linearly spaced voltage points from 3.17–4.2 V, enabling the straightforward data subtraction to obtain ΔQ(OCV) data [26]. The min-max normalization method was applied to process the ΔQ (OCV) data before feeding into the CNN, which retains the original distribution of the ΔQ(OCV) data and all transformed data fall into the range of [0,1]. The maximum and minimum values of the ΔQ(OCV) were kept constant during training, testing and diagnostics with experimental data.

6.5. Grad-CAM method

Gradient-weighted class activation mapping (Grad-CAM) is an interpretability technique that can be used to help understand the predictions made by a deep neural network [27]. The Grad-CAM is a generalization of the class activation mapping (CAM) technique, which is used to explore which parts of the input are most important for output identification. The Grad-CAM computes the importance map by taking the derivative of the regression output with respect to a convolutional feature map, i.e. a ReLU layer, which takes the output of a convolutional layer at the end of the network. The neuron importance weight (α_k^c) can be calculated as:

$$\alpha_k^c = \frac{1}{N}\sum_i \frac{\partial y^c}{\partial A_i^k} \quad (7)$$

where y^c, A_i^k, and N are the network output, representing the scalar value for regression c, the k feature maps (channels), with i indicating feature elements, and the total number of elements in the feature map, respectively. The weight α_k^c represents a partial linearization of the deep network downstream from A, and captures the 'importance' of feature map k for a target regression c.

The Grad-CAM is a weighted combination of the feature maps with an applied ReLU:

$$L^c_{\text{Grad-CAM}} = ReLU\left(\sum_k \alpha_k^c A^k\right) \quad (8)$$

We apply a ReLU to the linear combination of maps because we are only interested in the features that have a positive influence on the regression of interest. The calculation is therefore a coarse heat map of the same size as the feature map A and then can be up-sampled to the size of the input data. The places where this gradient is large are exactly the places where the final quantification depends most on the data.

6.6. Convolutional neural network

The CNN in Supplementary Fig. S3 contains eight learned layers: one input layer, five convolutional layers, one fully-connected layer, and one output layer. The first and second convolutional layers are the same, consisting of two arms, which contain 64 1 × 3 kernels with stride=2, and 64 1 × 5 kernels with stride=2, respectively. The identical third and fourth convolutional layers includes three arms, which contains 96 1 × 1 kernels with stride=2, 96 1 × 3 kernels with stride=2, and 96 1 × 5 kernels with stride=2. The four convolutional arms of the fifth convolutional layer are 256 1 × 1 kernels with stride=2, 256 1 × 1 kernels with stride=2 series connected to 256 1 × 3 kernels with stride=2, 256 1 × 1 kernels with stride=2 series connected to 256 1 × 5 kernels with stride=2, and 256 1 × 3 pooling kernels series connected to 256 1 × 1 kernels with stride=2. Each convolutional layer is with same-padding and followed by batch normalization and ReLU activation layers. They are concatenated, flattened and fed to five fully-connected layers. Each fully-connected layer contains 18,432 neurons and is connected to the regression output. The five outputs represent five independent DMs.

The synthetic dataset was randomly partitioned to 80% for training, and 20% for testing and the Adam optimizer [28] was utilized to train the CNN with a mini-batch of size 512 for 50 epochs, where the training processes are similar to the work [14]. The cost function (L_{loss}) for training the CNN can be described as:

$$L_{\text{loss}} = \sum_{j=1}^{5} \omega_j \cdot L_j, L_j = \frac{1}{2}\sum (Y_i - X_i)^2 \quad (9)$$

where ω_j, Y_i, and X_i stand for the weighting coefficient for every output, target values, and CNN predictions, respectively. We set the weighting coefficients as 1, 2, 8, 1, and 4 for LLI, LAM_{Gr}, LAM_{Si}, LAM_{PE} and RI, respectively. We used the RMS to evaluate the differences between the predicted and target values. All CNN training and testing for composite batteries were undertook in MATLAB on a single desktop computer with an NVIDIA Quadro P4000 GPU. The diagnostics with experimental data and the trained CNN was carried out in MATLAB on a single general computer with an Intel(R) Xeon(R) Silver 4110.

CRediT authorship contribution statement

Haijun Ruan: Writing – original draft, Writing – review & editing, Conceptualization, Methodology, Validation. **Niall Kirkaldy:** Writing – review & editing, Data curation, Formal analysis. **Gregory J. Offer:** Writing – review & editing, Supervision, Formal analysis. **Billy Wu:** Writing – review & editing, Supervision, Project administration, Conceptualization.

Declaration of competing interest

The authors declare that they have no known competing financial interests or personal relationships that could have appeared to influence the work reported in this paper

Data availability

Data will be made available on request.

Acknowledgements

This work was kindly supported by the EPSRC Impact Acceleration Award (EP/X52556X/1), the Faraday Institution's Industrial Fellowship (FIIF-013), the EPSRC Faraday Institution's Multi-Scale Modelling Project (EP/S003053/1, grant number FIRG003), the EPSRC Joint UK-India Clean Energy Center (JUICE) (EP/P003605/1) and the EPSRC Integrated Development of Low-Carbon Energy Systems (IDLES) project (EP/R045518/1).

Supplementary materials

Supplementary material associated with this article can be found, in the online version, at doi:10.1016/j.egyai.2024.100352.

References

[1] Liu Y, Zhang R, Wang J, Wang Y. Current and future lithium-ion battery manufacturing. IScience 2021;24(4):102332.
[2] Lyu Y, Liu Y, Yu Z-E, Su N, Liu Y, Li W, Li Q, Guo B, Liu B. Recent advances in high energy-density cathode materials for sodium-ion batteries. Sustain Mater Technol 2019;21:e00098.
[3] Goriparti S, Miele E, De Angelis F, Di Fabrizio E, Proietti Zaccaria R, Capiglia C. Review on recent progress of nanostructured anode materials for Li-ion batteries. J Power Source 2014;257:421–43.
[4] Ding Y, Cano ZP, Yu A, Lu J, Chen Z. Automotive Li-ion batteries: current status and future perspectives. Electrochem Energy Rev 2019;2:1–28.

[5] Wang C, Amietszajew T, Carvajal R, Guo Y, Ahmed Z, Zhang C, Goodlet G, Bhagat R. Cold ageing of nmc811 lithium-ion batteries. Energies 2021;14(16):4724.
[6] Anseán D, Baure G, González M, Cameán I, García AB, Dubarry M. Mechanistic investigation of silicon-graphite/LiNi0. 8Mn0. 1Co0. 1O2 commercial cells for non-intrusive diagnosis and prognosis. J Power Source 2020;459:227882.
[7] Markus S, Sturm J, Ludwig S, Schmitt J, Jossen A. Evolution of initial cell-to-cell variations during a three-year production cycle. ETransportation 2021;8:100102.
[8] Steffen B, Heugel P, Kessel Ovon, Commerell W, Tübke J. Influence of charging protocols on the charging capability and aging of lithium-ion cells with silicon-containing anodes. J Energy Storage 2022;49:104044.
[9] Niall K, Samieian MA, Offer GJ, Marinescu M, Patel Y. Lithium-ion battery degradation: measuring rapid loss of active silicon in silicon–graphite composite electrodes. ACS Appl Energy Mater 2022;5(11):13367–76.
[10] Tian J, Xiong R, Shen W, Sun F. Electrode ageing estimation and open circuit voltage reconstruction for lithium ion batteries. Energy Storage Mater 2021;37:283–95.
[11] Yang S, Zhang C, Jiang J, Zhang W, Gao Y, Zhang L. A voltage reconstruction model based on partial charging curve for state-of-health estimation of lithium-ion batteries. J Energy Storage 2021;35:102271.
[12] Marongiu A, Nlandi N, Rong Y, Sauer DU. On-board capacity estimation of lithium iron phosphate batteries by means of half-cell curves. J Power Source 2016;324:158–69.
[13] Schmitt J, Rehm M, Karger A, Jossen A. Capacity and degradation mode estimation for lithium-ion batteries based on partial charging curves at different current rates. J Energy Storage 2023;59:106517.
[14] Ruan H, Chen J, Ai W, Wu B. Generalised diagnostic framework for rapid battery degradation quantification with deep learning. Energy AI 2022;9:100158.
[15] Birkl CR, Roberts MR, McTurk E, Bruce PG, Howey DA. Degradation diagnostics for lithium ion cells. J Power Source 2017;341:373–86.
[16] Edge JS, O'Kane S, Prosser R, Kirkaldy ND, Patel AN, Hales A, Ghosh A, et al. Lithium ion battery degradation: what you need to know. Phys Chem Chem Phys 2021;23(14):8200–21.
[17] Ai W, Kirkaldy N, Jiang Y, Offer G, Wang H, Wu B. A composite electrode model for lithium-ion batteries with silicon/graphite negative electrodes. J Power Source 2022;527:231142.
[18] Zhao K, Pharr M, Wan Q, Wang WL, Kaxiras E, Vlassak JJ, Suo Z. Concurrent reaction and plasticity during initial lithiation of crystalline silicon in lithium-ion batteries. J Electrochem Soc 2011;159(3):A238.
[19] Kabir MM, Demirocak DE. Degradation mechanisms in Li-ion batteries: a state-of-the-art eview. Int J Energy Res 2017;41(14):1963–86.
[20] Ruan H, Varela Barreras J, Engstrom T, Merla Y, Millar R, Wu B. Lithium-ion battery lifetime extension: a review of derating methods. J Power Source 2023;563:232805.
[21] Li D, Li H, Danilov D, Gao L, Zhou J, Eichel R-A, Yang Y, Notten PHL. Temperature-dependent cycling performance and ageing mechanisms of C6/LiNi1/3Mn1/3Co1/3O2 batteries. J Power Source 2018;396:444–52.
[22] Kirkaldy, N., M.A. Samieian, G.J. Offer, M. Marinescu, and Y. Patel. Data. https://zenodo.org/record/7235858.
[23] Chen J, Marlow MN, Jiang Q, Wu B. Peak-tracking method to quantify degradation modes in lithium-ion batteries via differential voltage and incremental capacity. J Energy Storage 2022;45:103669.
[24] Hamby DM. A review of techniques for parameter sensitivity analysis of environmental models. Environ Monit Assess 1994;32:135–54.
[25] Ruan H, Sun B, Zhang W, Su X, He X. Quantitative analysis of performance decrease and fast-charging limitation for lithium-ion batteries at low temperature based on the electrochemical model. IEEE Transact Intell Transport Syst 2020;22(1):640–50.
[26] Severson KA, Attia PM, Jin N, Perkins N, Jiang B, Yang Z, Chen MH, et al. Data-driven prediction of battery cycle life before capacity degradation. Nat Energy 2019;4(5):383–91.
[27] Selvaraju RR, Cogswell M, Das A, Vedantam R, Parikh D, Batra D. Grad-cam: visual explanations from deep networks via gradient-based localization. In: Proceedings of the IEEE international conference on computer vision; 2017. p. 618–26.
[28] Kingma, D.P., and J. Ba. "Adam: a method for stochastic optimization." arXiv preprint arXiv:1412.6980 (2014).